An epitaxial surface heterostructure anchoring approach for high-performance Ni-rich layered cathodes

Weili Sun[a], Qingqing Zhang[a,*], Xiao-Guang Sun[b], Cheng Li[c], Yongsheng Huang[a], Wenyu Mu[a], Junbin Tan[a], Jianlin Li[d,*], Kai Liu[e,*], Shijian Zheng[a], Sheng Dai[b,f]

[a] *Tianjin Key Laboratory of Materials Laminating Fabrication and Interface Control Technology, School of Materials Science and Engineering, Hebei University of Technology, Tianjin 300130, China*

[b] *Chemical Sciences Division, Oak Ridge National Laboratory, Oak Ridge, TN 37831, USA*

[c] *Neutron Scattering Division, Oak Ridge National Laboratory, Oak Ridge, TN 37830, USA*

[d] *Applied Materials Division, Argonne National Laboratory, Lemont, IL 60439, USA*

[e] *School of Materials Science and Engineering, Tianjin University of Technology, Tianjin 300384, China*

[f] *Department of Chemistry, University of Tennessee, Knoxville, TN 37996, USA*

[*]Corresponding authors.

E-mail addresses: zqq055@163.com (Q. Zhang), jianlin.li@anl.gov (J. Li), liukai_tju_edu_cn@163.com (K. Liu).

ABSTRACT

Nickel-rich (Ni≥90%) layered oxides materials have emerged as a promising candidate for next-generation high-energy-density lithium-ion batteries (LIBs). However, their widespread application is hindered by structural fatigue and lattice oxygen loss. In this work, an epitaxial surface rock-salt nanolayer is successfully developed on the $LiNi_{0.9}Co_{0.1}O_2$ sub-surface via heteroatom anchoring utilizing high-valence element molybdenum modification. This in-situ formed conformal buffer phase with a thickness of 1.2 nm effectively suppresses the continuous interphase side-reactions, and thus maintains the excellent structure integrity at high voltage. Furthermore, theoretical calculations indicate that the lattice oxygen reversibility in the anion framework of the optimized sample is obviously enhanced due to the higher content of O 2*p* states near the Fermi level than that of the pristine one. Meanwhile, the stronger Mo–O bond

further reduces cell volume alteration, which improves the bulk structure stability of modified materials. Besides, the detailed charge compensation mechanism suggests that the average oxidation state of Ni is reduced, which induces more active Li^+ participating in the redox reactions, boosting the cell energy density. As a result, the uniquely designed cathode materials exhibit an extraordinary discharge capacity of 245.4 mAh g^{-1} at 0.1 C, remarkable rate performance of 169.3 mAh g^{-1} at 10 C at 4.5 V, and a high capacity retention of 70.5% after 1000 cycles in full cells at a high cut-off voltage of 4.4 V. This strategy provides an valuable insight into constructing distinctive heterostructure on high-performance Ni-rich layered cathodes for LIBs.

Keywords: Ni-rich layered oxides; Rock-salt nanolayer; Heteroatom anchoring; Lattice oxygen reversibility; Lithium-ion batteries

1. Introduction

With the rapid development of portable electronics, electric vehicles, and energy storage devices, the demand for lithium-ion batteries (LIBs) with high energy/power density and long cycle life has dramatically increased [1-3]. Ni-rich (≥90%) layered oxide cathode materials, such as $LiNi_{1-x-y}Co_xMn_yO_2$ (NCM), have received tremendous attentions due to its improved energy density, enviable life span, and cost-effectiveness [4-6]. However, numerously detrimental effects are inevitably incurred with the increment of Ni content, including crystal structure reconstruction [7], electrolyte/electrode interphase exacerbation [8], and lattice oxygen loss [9]. These fatal drawbacks provoke serious structure instability, and thus accelerate its capacity decay and rate performance deterioration, which further hinder the practical application of high-Ni cathode materials in LIBs.

Heterostructure construction is considered as an effective approach to ameliorating the electrochemical performance of NCM cathode [10-12]. It is usually achieved by pre-forming a nanoscale cation-mixed layer (rock salt phase or spinel-type structure) on the surface of material while retaining the core region with typically layered structure indexed into *R*-3*m* space. The

generated buffer phase, sharing the identical oxygen sub-lattice with the bulk layered matrix, displays good structural compatibility with the host framework [13]. Therefore, it can obviously reduce the local stress-stain and intergranular and intragranular microcracks formation, and effectively maintain the structural integrity of the cathode particles during the long-term cycling process [14]. Besides, the epitaxial growth shell layer can effectively suppress the notorious parasitic reactions with electrolytes and transition metal ion dissolution, which alleviate the continuously harmful phase transformation [15]. Many efforts on building different robust microstructures have seen significant progress for NCM materials in improving their cycling stability. For instance, a spinel mortise-tenon heterostructure was introduced into the layered NCM cathode materials, and this bizarre construction suppressed the adversely anisotropic volume variations, and thus improved its mechanochemical stability [16]. An epitaxial coexistence Li/Ni disordered layer on NCM sub-surface effectively mitigated the irreversible phase transitions and retarded particle pulverization [17]. A rock salt phase with *Fm*-3*m* space structure was induced by W-doping NCM, which not only reduced the interphase side reactions with electrolytes, but also enhanced the capacity retention upon the prolonged cycling process [18]. These are mainly attributed to the dramatically improved structural stability, ensuring its grain integrity due to the pillar effect. However, the above results are contradicted with previous reports that Li/Ni mixing induced heterogeneous phase usually aggravates the particle microcrack formation and accelerates the structural collapse of materials [19-21]. Therefore, a comprehensive insight into the in-depth impact mechanism of heterostructure construction on bulk structure-property relationship, especially for the crystalline structure evolution, Li^+ transfer kinetics and charge compensation mechanism is essential to shed light on these controversies.

In this study, we design an ultrathin rock salt phase shell with conformal decoration on layered $LiNi_{0.9}Co_{0.1}O_2$ cathode material by inducing an appropriate amount of Li/Ni mixing via incorporation of high-valence Mo^{6+} during the lithiation process. Experimental results and

theoretical calculations reveal that heterostructure construction can prominently enhance the reversibility of the lattice oxygen and reduce cell volume alteration, thus maintaining the structure integrity of the materials. The detailed evolution of crystalline structure is unveiled utilizing the synchrotron-based X-ray powder diffraction, neutron powder diffraction, in-situ X-ray diffraction, and high-angle annular dark-field scanning transmission electron microscopy. X-ray absorption fine structure and X-ray photo electron spectroscopy further elucidate the charge compensation mechanism of the optimized sample that the average oxidation state of Ni is reduced, which induces more active Li^+ participating in the redox reactions. Thus, the distinctively developed method enables the formed cathode materials with an outstanding discharge capacity of 245.4 mAh g^{-1} at 0.1 C, an excellent rate performance of 169.3 mAh g^{-1} at 10 C at 4.5 V, and a high capacity retention up to 70.5% after 1000 cycles in coin-type full cells at a voltage range of 2.7–4.4 V. This modification strategy opens a new avenue to build a robust interphase heterostructure for high-performance cathode materials of LIBs.

2. Experimental

2.1. Material synthesis

The samples were synthesized by uniformly mixing the Ni-rich $Ni_{0.9}Co_{0.1}(OH)_2$ precursor (Tianjin Bamo Technology Co., Ltd), $LiOH·H_2O$ (99.0%, Aladdin), and MoO_3 dopant (99.95%, Aladdin) with anhydrous ethanol as the dispersant at a molar ratio of Li: Mo: (Ni+Co) = 1.05: x: (1−x) (x = 0.0025, 0.005, 0.0075, and 0.01) and then dried at 60 °C. Then the obtained mixtures were calcined in a tube furnace at 700 °C for 10 h under an oxygen atmosphere, with a heating rate of 5 °C min^{-1}, and finally naturally cooled to room temperature. The resulting materials were labeled as NC90 (T) and Mo-NC90 (T) (T = 700/730/750) for the pristine and modified samples based on different calcination temperatures. Mo-NC90 (T) (T = 700/730/750) materials have a Mo doping atomic level of 0.5%.

2.2. Material characterizations

Neutron powder diffraction (NPD) data were collected at the NOMAD diffractometer at

the Spallation Neutron Source (SNS), Oak Ridge National Laboratory. Approximately 100 mg of sample was loaded into 3 mm diameter quartz capillaries with about 20 mm in height, in the N_2-filled glovebox. Data were collected for approximately 1 h, covering the *d* space from 0.20 to 12.0 Å. For the Rietveld analysis, the peak profile was obtained by refining a SRM Si 640d. Refinement was carried out using TOPAS 6 [22].

Synchrotron radiation X-ray diffraction (SXRD) experiments were carried out at the beamline BL14B of Shanghai Synchrotron Radiation Facility (SSRF) with a constant wavelength of 0.6889 Å and the data were acquired in the 2θ ranging from 1° to 40°. The specimens were put into a sealed 0.5 mm-diameter boron-rich capillary glass tubes in an Ar-filled glove box.

Both samples show *hkl* dependent anisotropic broadening, and thus the peak profile of both the SXRD and NPD data were described by the convolution of the Stephens's anisotropic broadening model with the respective instrument resolution [22]. The anisotropic broadening parameters S004, S400, and S202 are highly correlated and thus only S202 was used in the refinement.

During the structural analysis, it was assumed that the only type of defects is the Li-Ni antisite defects. Their corresponding site occupancies and isotropic site atomic displacement parameters (ADPs) were constrained accordingly. The occupancy of Co at the TM site was fixed at 0.1.

The crystal structures of all materials were characterized by X-ray diffraction (XRD, Rigaku SmartLabm, Cu K_α radiation, λ = 1.5406Å), over the 2θ range of 10°–90° with a scanning rate of 6° min^{-1}. The collected XRD data were refined using the General Structure Analysis System (GSAS-ii). In situ XRD was conducted in a specialized in situ XRD cell (LIB-XRD, Beijing Scistar Technology Co., Ltd, China). The detailed morphology and microstructure of powder samples and cycled electrode were characterized using scanning electron microscopy (SEM, JSM-7610F), high-angle annular dark-field scanning transmission

electron microscopy (HAADF-STEM, JEM-ARM200F), and TEM (JEM-2100F). The oxidation states of different elements on the surface of prepared powder and cycled electrodes with different etching depths were determined by X-ray photoelectron spectroscopy (XPS, Thermo Fisher Scientific K-Alpha$^+$) with an Al K_α radiation. The collected data were calibrated against the C 1*s* peak at 284.8 eV. The X-ray absorption fine structure (XAFS) measurements were performed to detect the valence state and the coordination environment of Ni and Co species (XAFS-500-A, Anhui Specreation Instruments Co., Ltd, China). The obtained spectra were processed by ATHENA and extended X-ray absorption fine structure (EXAFS) spectra were fitted using ARTEMIS in Demeter software package.

All density functional theory (DFT) calculations were conducted using the Vienna Ab initio Simulation Package (VASP) [23,24]. The exchange-correlation potential was described by the Perdew-Burke-Ernzerhof (PBE) generalized gradient approximation (GGA) [25]. Electron-ion interactions were modeled by the projector augmented wave (PAW) method [26]. The calculations employed cut-off energy of 400 eV, and the Brillouin zone was sampled with a 2 × 2 × 1 *k*-point grid. The energy and force convergence criteria for the self-consistent iterations were set to 10^{-4} eV and 0.02 eV Å^{-1}, respectively. Additionally, the DFT + U correction was applied for Ni, Co, and Mo atoms, with *U-J* values of 3.00, 4.91, and 3.50 eV, respectively. The DFT-D3 method was used to account for van der Waals (vdW) interactions [27].

The binding energies (E_b) of O in the $LiNiCoO_2$ systems were calculated by Eq. (1).

$$E_b = E_{LiNiCoO2\text{-}Ov} + E_O - E_{LiNiCoO2} \quad (1)$$

where $E_{LiNiCoO2\text{-}Ov}$ and $E_{LiNiCoO2}$ were the total energies of $LiNiCoO_2$-Ov and $LiNiCoO_2$ system, respectively. E_O was the energy of the single atom O.

2.3. Electrochemical tests

For the preparation of cathode, active material, conductive agent (Super P, Canrud), and binder (polyvinylidene difluoride, PVDF, DoDo) were mixed at a weight ratio of 90: 5.5: 4.5 in *N*-methyl-2-pyrrolidone (NMP, DoDo) to obtain a homogeneous slurry. The slurry was

coated onto aluminum current collector and dried overnight at 80 °C under vacuum. The cathode was then cut into disks with a diameter of 12 mm, with an average active material loading of approximately 1.5–2.5 mg cm^{-2}. Coin-type cells (CR2032) were assembled in a glove box ($O_2 \leq$ 0.01 ppm, $H_2O \leq$ 0.01 ppm) using Li metal as the anode, a polypropylene/polyethylene/polypropylene (PP/PE/PP, Celgard 2325) as the separator, and 1.2 M $LiPF_6$ in ethylene carbonate/ethyl methyl carbonate (EC/EMC, *V*/*V* = 3/7) with 2 wt% additive of fluorinated ethylene carbonate (FEC) as the electrolyte (Jinniu Power Materials of Tianjin Co., Ltd). Charge-discharge tests of half cells were conducted utilizing a LANHE testing system at different current densities (1.0 C = 200 mA g^{-1}) with a voltage range of 2.7–4.5 V. Cyclic voltammetry (CV) tests with scan rates from 0.1 to 1 mV s^{-1} at 2.7–4.5 V and electrochemical impedance spectroscopy (EIS) tests over a frequency range of 0.01 Hz to 100 kHz with a voltage amplitude of 10 mV were performed on a CHI 660 electrochemical workstation. Galvanostatic intermittent titration technique (GITT) tests were conducted at 0.1 C for 15 min, followed by a rest time of 30 min.

The diffusion coefficient of Li^+ in the cathode materials after 500 cycles was measured through GITT tests. D_{Li^+} was calculated using the following Eq. (2) [28].

$$D_{Li^+} = \frac{4}{\pi\tau}\left(\frac{m_B V_m}{M_B A}\right)^2 \left(\frac{\Delta E_s}{\Delta E_t}\right)^2 \quad (2)$$

In this equation, D_{Li^+} represents the diffusion coefficient of Li^+ ions, τ is the applied time under constant current, m_B denotes the mass of the electrode, V_m is the molar volume of the electrode, M_B represents the molar mass of the electrode, A refers to the contact area between the electrode and the electrolyte, ΔE_s is the voltage difference between the steady-state potentials before and after the current pulse, and ΔE_t is the total voltage difference under constant current application.

Meanwhile, the D_{Li^+} is further checked by CV tests under different scan rates according to the Randles-Sevcik equation (Eq. (3)) [29].

$$I_{\mathrm{p}} = 2.69 \times 10^5 n^{3/2} A^{1/2} D^{1/2} C v^{1/2} \quad (3)$$

Here, I_{p} represents the peak current (A mg^{-1}), n is the number of electrons involved in the redox reaction, A denotes the geometrical surface area of the electrode (cm^2), D is the diffusion coefficient (cm^2 s^{-1}), C refers to the lithium-ion concentration (mol cm^{-3}), and v is the scan rate (V s^{-1}).

To assemble the full cell, commercial graphite and PVDF were mixed at 9:1 (wt%) ratio in NMP to form a uniform slurry. This slurry was coated onto copper current collector and dried overnight in a vacuum at 100 °C. The anode was cut into 12 mm diameter disks. The capacity ratio of anode/cathode was approximately 1.1:1.

3. Results and discussion

3.1. Surface heterostructure construction

NPD was carried out for NC90 (700) and Mo-NC90 (730) to examine their crystal structure, as depicted in Fig. 1(a and b) and Figs. S1 and S2. The Rietveld refinement results demonstrate that the structure of both cathode materials can be well indexed to the hexagonal α-$NaFeO_2$-type structure with a space group of *R*-3*m* [30]. According to the obtained refinement data (Tables S1 and S2), the modified Mo-NC90 (730) displays a slightly higher Li-Ni antisite defect concentration of 1.3%, compared to 1.1% of the pristine NC90 (700). SXRD was further conducted to detect the crystal structure of Mo-NC90 (730), as shown in Fig. 1(c) and Fig. S3. The SXRD results also indicate that Mo-NC90 (730) has a higher antisite defect than the pristine one, which is consistent with the NPD result. Besides, the influence of calcination temperature of the Mo doped samples on antisite defect concentration was also investigated by XRD (Fig. S4 and Table S3). It is observed that Li/Ni mixing increases with the elevation of lithiation temperature for the Mo-modified materials. Comparatively, the Mo-NC90 (730) material exhibits a higher Li/Ni mixing compared to other samples, with a peak intensity ratio of $I_{(003)}/I_{(104)}$ of approximately 1.25. This is probably ascribed to the increased lithiation temperature and high valence Mo^{6+} ions doping, which synergistically facilitates the reduction

of Ni^{3+} to Ni^{2+} [31-33].

To further validate the structure stability of the designed heterostructure construction, the formation energies (E_f) of three different models were calculated by first principle calculation, as shown in Fig. 1(d). E_f of $Li_{30}Ni_{26}Co_3Mo_1O_{60}$ (Model 2) is 3.11 eV lower than that of the pristine $Li_{30}Ni_{27}Co_3O_{60}$ (Model 1). After introducing one Li/Ni antisite around Mo atom to form $Li_{30}Ni_{26}Co_3Mo_1O_{60}$, E_f of Model 3 is about 3.27 and 0.16 eV lower than that of Model 1 and Model 2, respectively. It indicates that E_f decreases with antisite introduction upon Mo doping, confirming the improved structure stability of Li/Ni intermixing heterostructure configuration (Model 3) [34]. Furthermore, the three structural models were further constructed to investigate the effects of heterostructure configuration on binding energy of the two O atoms O1/O2 in the surface/bulk phase, as shown in Fig. 1(e–g). The binding energies of the O1 atom on the surface and the O2 atom in the bulk phase of the materials were further calculated by the three different models to analyze the influence of heterostructure configuration on its lattice oxygen and structural stability. The binding energies of O1 and O2 in the model with Mo doping inducing Li/Ni mixing are calculated as 3.233 and 3.857 eV, respectively. The highest value among the three models suggests that the lattice oxygen is more difficult to escape from the surface of the heterostructure construction (Model g). The higher binding energies can decelerate the oxidation of oxygen atoms as a more stable anion framework, which is beneficial to improving the crystal structure stability of the sample during the electrochemical cycling process [34].

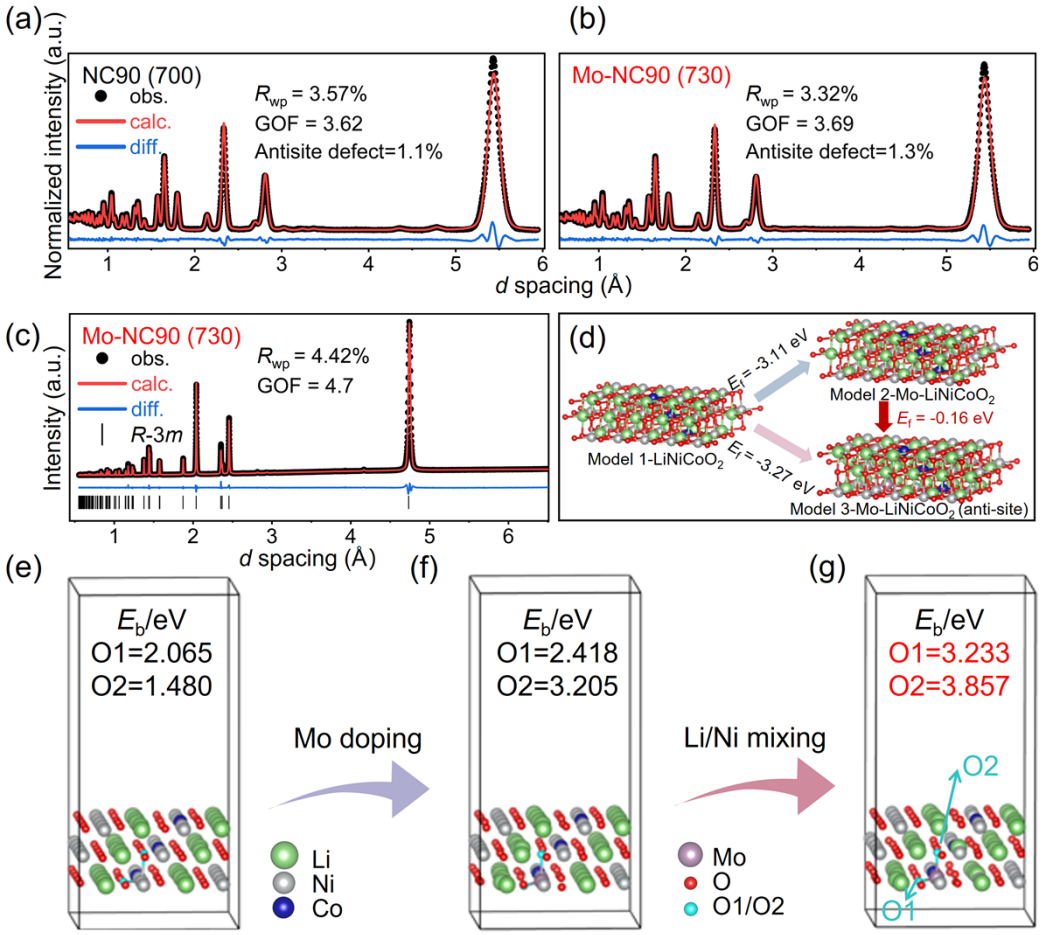

Fig. 1. The NPD spectra of (a) NC90 (700) and (b) Mo-NC90 (730). (c) SXRD and corresponding Rietveld refinement results of Mo-NC90 (730). (d) First principles computational formation energies of structural model. (e) Structure model of $Li_{30}Ni_{27}Co_3O_{60}$ based on $LiNiCoO_2$ constructed by (104) plane, (f) $Li_{30}Ni_{26}Co_3Mo_1O_{60}$, and (g) $Li_{30}Ni_{26}Co_3Mo_1O_{60}$ with Li/Ni antisite around Mo atom. Insets are the calculated binding energy of two O atoms O1/O2 in the surface/bulk phase.

The grain morphology of both cathode materials was examined by SEM, as shown in Fig. S5. Both NC90 (700) and Mo-NC90 (730) exhibit similar spherical shape and particle size. The corresponding energy-dispersive spectroscopy (EDS) elemental mapping implies the uniform distribution of Ni, Co, O, and Mo elements on the particle surface of Mo-NC90 (730) (Fig. S6). Further investigation on the local surface structures of NC90 (700) and Mo-NC90 (730) was conducted using high-resolution TEM (HRTEM). The pristine NC90 (700) presents the typical layered structure from the surface to the bulk (Fig. 2a). Line-profile analysis of area 1 and area

2 further proves the identical lattice distance, indexed to the *R*-3*m* space group [35]. However, the surface structure of Mo-NC90 (730) is obviously different from its bulk, as shown in Fig. 2(b). The inner bulk remains a well-defined ordered layered structure (area 1 in Fig. 2b), while its surface exhibits an obviously different interplanar spacing (area 2 in Fig. 2b), suggesting that some transition metal ions may have migrated to the octahedron lattice sites occupied by lithium atom. This finding is also corroborated by the selected-area electron diffraction (SAED) pattern (Fig. S7).

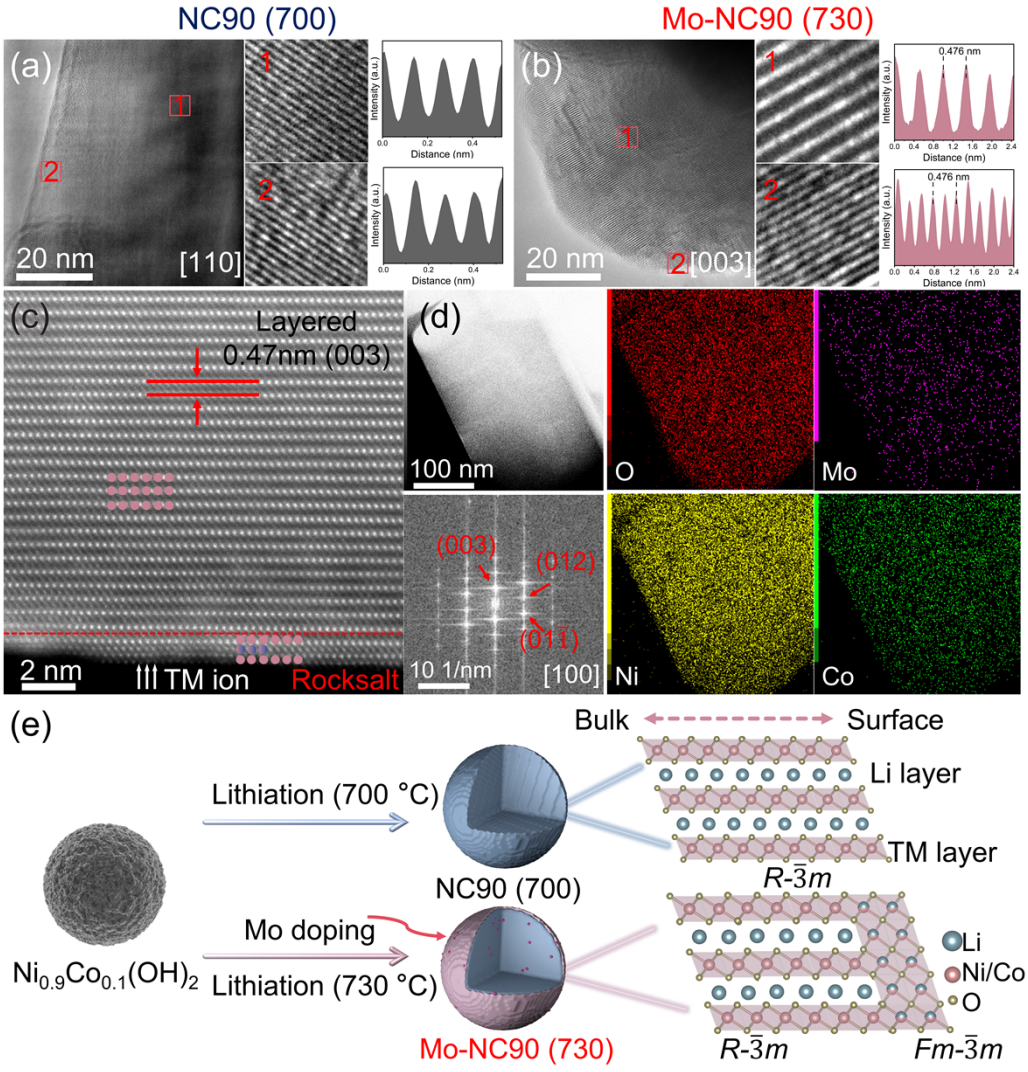

Fig. 2. The HRTEM images of (a) NC90 (700) in [110] axis and (b) Mo-NC90 (730) in [003] axis, the inset is the enlarged images in selected areas and a line profile analysis of the magnified lattice spacing at the corresponding regions. (c) HAADF-STEM images of Mo-NC90 (730). (d) EDS elemental mapping of Mo-NC90 (730) and corresponding fast Fourier transform (FFT)

patterns. (e) Schematic illustration of structure evolution mechanism during the preparation of NC90 (700) and Mo-NC90 (730) materials.

HAADF-STEM was further utilized to confirm the crystal structure variations for Mo-NC90 (730), as depicted in Fig. 2(c). The lattice fringe with 0.47 nm corresponding to the (003) plane of the *R*-3*m* structure is identified [35], demonstrating that the typical layered structure is well retained in the bulk region. Its surface exhibits an ordered *Fm*-3*m* rock salt phase with a thickness of 1.2 nm. Additionally, similar structure can also be observed in other regions of Mo-NC90 (730), as shown in Fig. S8. The formation of the surface phase reconstruction is attributed to the high-valence Mo^{6+} ion doping, which will promote the partial reduction of Ni^{3+} to Ni^{2+} to ensure charge balance [31]. This leads to mutual diffusion of Li^{+} and Ni^{2+}, thus forming Li/Ni intermixing [36]. This unique occupation of Ni^{2+} into the Li layer plays a pillar function to mitigate the unfavorable structure collapse. Essentially, the heterostructure construction layer is immunized against electrolyte corrosion during the long-term cycling process, potentially enhancing the electrochemical performance [12]. The Mo-modified cathode is verified by the homogeneous elemental distribution (Fig. 2d). Fig. 2(e) depicts the structure evolution mechanism of NC90 (700) and Mo-NC90 (730) during the synthesis process. Compared to the pristine sample, the fabrication of Mo-NC90 (730) is successfully achieved via Mo doping with increasing lithiation temperature. An ultra-thin *Fm*-3*m* rock-salt layer with conformal coating on the surface of Mo-NC90 (730) is generated, which will reduce electrolyte corrosion, thereby improving its structure stability.

3.2. Charge compensation mechanism

The local electronic structure variations induced via the heterostructure construction were explored by the density of state (DOS), as shown in Fig. 3(a and b). It can be found that the electronic states of both cathodes mainly arise from the Ni *d* and O *p* orbitals hybridization. Notably, Mo-NC90 (730) shows some new peaks in the energy range from 1.7 to 3.0 eV, indicating a slight lattice distortion triggered by the introduction of Mo with greater

electronegativity than Ni/Co ions [37]. From this diagram, it can be found that the band gap of Mo-NC90 (730) is significantly lower than that of NC90 (700), implying a higher electronic conductivity for the modified cathode and potentially improving its rate performance [38]. In addition, Mo-NC90 (730) demonstrates a higher content of O 2*p* states near the Fermi level, suggesting that the lattice-oxygen stability is enhanced owing to the stronger bond of Mo–O than Ni/Co–O [39]. Due to the high oxidation state of Mo^{6+}, its doping induces charge redistribution of Ni ions to maintain charge neutrality, which will be further elaborated in the subsequent sections [31].

To explore the impact of heterophase structure on the valence states and local geometric structures of Ni and Co elements in the samples, X-ray absorption near-edge structure (XANES spectra were measured, as shown in Fig. 3(c–h). The normalized Ni *K*-edge spectra (Fig. 3c) display that the pre-edge and near-edge energies of Mo-NC90 (730) shift towards lower energy (leftward shift) compared to NC90 (700), indicating a reduction in the average oxidation state of Ni in the NC90 system upon Mo element incorporation [40]. The higher content of Ni^{2+} in Mo-NC90 (730), typically associated with higher discharge specific capacity in the cathode material, will be further validated in the subsequent electrochemical testing [41]. In Fig. 3(d), the Fourier-transformed (FT) EXAFS spectrum of the Ni *K*-edge reveals the relationship of Ni with O and transition metal ions (TM) [42]. In the first coordination shell, the Ni–O peak intensity of NC90 (700) is lower, indicating the average oxidation state of Ni closer to trivalent. The more content of Ni^{3+} is easy to trigger the distortion of NiO_6, due to its low-spin state $t_{2g}^6 e_g^1$ electronic configuration (Jahn-Teller effect) [43]. However, this phenomenon is significantly mitigated in Mo-NC90 (730), resulting from the increased peak intensity of the coordination shell. The lowered Ni valence state can effectively improve the structure stability of Mo-NC90 (730). Furthermore, complementary analyses of the EXAFS data on atomic coordination environment and bond lengths using wavelet transform technique in conjunction with FT transformation were performed. As shown in Fig. 3(e and f), the local structure around Ni atoms

remains unchanged, yet the bond lengths in NC90 (700) are slightly shorter than those in Mo-NC90 (730), indicating more Ni^{2+} in Mo-NC90 (730), consistent with the above results [44]. In the XANES and EXAFS spectra at Co *K*-edge (Fig. 3g and h), a comparative shift towards higher oxidation states of Co can be observed in Mo-NC90 (730) in order to maintain charge neutrality.

XPS was employed to further analyze the elemental oxidation states in both materials after being calibrated by the C-C peak in the C 1*s* spectra (Fig. S9). Fig. 3(i) presents the characteristic peaks of Ni 2*p* appearing Ni $2p_{3/2}$ and Ni $2p_{1/2}$ [45]. The proportions of Ni^{2+} and Ni^{3+} can be deduced from the peak areas. Compared to NC90 (700), Mo-NC90 (730) exhibits a higher Ni^{2+} content (26.5% vs. 35.7%), consistent with the increased Li/Ni mixing observed in Mo-NC90 (730) through SXRD and NPD. Ni^{3+} is a Jahn-Teller active ion, and the reduced content in Mo-NC90 (730) will inhibit its irreversible phase transition, which aligns well with the XAFS results. The three peaks in the O 1*s* spectrum are attributed to absorbed oxygen, oxygen deposited species (Li_2CO_3 or LiOH), and lattice oxygen [40]. Peaks corresponding to lattice oxygen are observed at 528.8 eV for Mo-NC90 (730) and 528.6 eV for NC90 (700). The binding energy of lattice oxygen in the Mo-doped samples shifts to higher energy due to the formation of stronger Mo–O bonds, leading to a more stable anion framework on the material surface and thereby enhancing its cycling stability [45]. Furthermore, the proportion of lattice oxygen in Mo-NC90 (730) is larger, further confirming the results. Lastly, the emergent characteristic peaks of Mo are detected in the modified material [46], providing the evidence for successful incorporation of Mo elements.

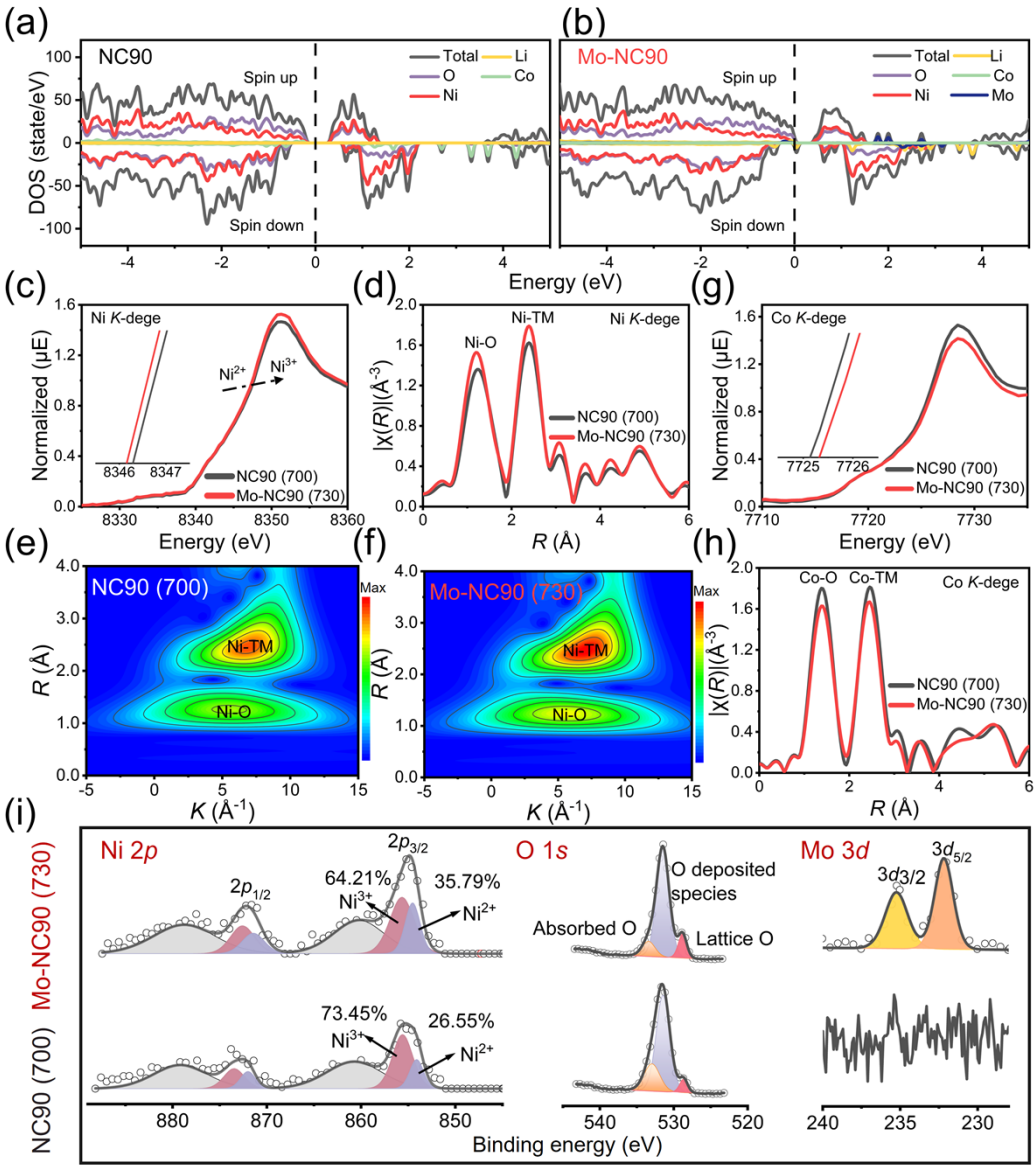

Fig. 3. Calculated DOS for (a) pristine and (b) Mo modified NC90. (c) XANES and (d) EXAFS spectra at Ni *K*-edge for NC90 (700) and Mo-NC90 (730). Wavelet-transformed Ni *K*-edge EXAFS spectra of (e) NC90 (700) and (f) Mo-NC90 (730). (g) XANES and (h) EXAFS spectra at Co *K*-edge for NC90 (700) and Mo-NC90 (730). (i) XPS spectra of Ni 2*p*, O 1*s*, and Mo 3*d* for both cathode materials.

3.3. Electrochemical performance

To understand the effects of heterostructure regulation on the material performance, the electrochemical tests of both NC90 (700) and Mo-NC90 (730) were investigated, as shown in Fig. 4. From their charge-discharge profiles and dQ/dV curves (Fig. 4a), a specific capacity of

188.5 mAh g^{-1} is obtained for NC90 (700) during the first charge process, corresponding to 0.71 mol extracted Li. Notably, there is 0.75 mol extracted Li (202.4 mAh g^{-1}) for the modified material, demonstrating a higher capacity of the integrated heterostructure due to increasing content of active Ni^{2+}. Excess Ni^{2+}, oxidized to Ni^{3+}/Ni^{4+}, can adjust valence charge distribution of the surrounding ions. Therefore, more Li^+ can be extracted and inserted into the host. Meanwhile, the significantly decreased voltage drops from the dQ/dV curves at different cycles indicate that the pre-formed architecture can improve its interphasial compatibility and structural stability upon the long-term cycling process [47]. There is a large polarization of 0.29 V for NC90 (700), significantly higher than 0.19 V for Mo-NC90 (730) after 250 cycles. Besides, an activation over-potential in pristine NC90 (700) is evidenced by the break of curves. However, it is absent from the modified sample, indicating a faster Li^+ mobility and less irreversible phase degradation [48]. The higher phase transition reversibility observed from 4.1 to 4.2 V (Fig. S10) in Mo-NC90 (730) also demonstrates its much-improved electrochemical properties.

GITT was utilized to calculate Li^+ diffusion coefficient (D_{Li^+}) of the two cathode materials after 500 cycles, as illustrated in Fig. 4(b). The D_{Li^+} of Mo-NC90 (730) is approximately 10^{-10} cm^2 s^{-1}, significantly higher than that of NC90 (700). The heterostructure regulation on Mo-NC90 (730) can not only reduce electrochemical polarization, but also enhance Li^+ transfer kinetics from the surface to the bulk. Meanwhile, the D_{Li^+} is further checked by CV tests under different scan rates (Fig. S11), which are also consistent with the GITT results.

The cycling performances of different cathodes were evaluated under a high cut-off voltage (4.5 V vs. Li/Li^+), as depicted in Fig. 4(c). Mo-NC90 (730) demonstrates both higher specific capacity (202.4 mAh g^{-1}) and retention rate (74.1%) than NC90 (700) (188.5 mAh g^{-1}, 41.8%) after 500 cycles. The discharge capacity of Mo-NC90 increases slowly in the initial cycles due to delayed activation [49]. The superior cycling stability of Mo-NC90 (730) can also be observed at the current densities of 5 and 1 C (Figs. S12–S14). The rate performances of both

samples were further tested at different current densities from 0.1 to 10 C, as shown in Fig. 4(d) and Fig. S15. The Mo-NC90 (730) exhibits a high discharge capacity of approaching 166.5 mAh g^{-1}, significantly surpassing that of the NC90 (700) (144.8 mAh g^{-1}) under the 10 C rate. Even working at a high temperature of 60 °C, the cycling stability of Mo-NC90 (730) outperforms the pristine one (Fig. S16). Meanwhile, the effects of lithiation temperature and doping content on the electrochemical performance of the materials are also investigated (Figs. S12–S18). The results show that the optimal lithiation temperature and doping concentration for the modified cathode is 730 °C and 0.5 mol%, respectively. EIS was then carried out to examine the interphase evolution of electrodes during the cycling processes (Fig. 4e, Fig. S19 and Table S4). It shows that Mo-NC90 (730) presents a reduced variation value of charge transfer resistance (R_{ct}). After 500 cycles, the Mo-NC90 (730) shows a lower R_{ct} of 143.3 Ω in comparison to 201.1 Ω of NC90 (700). It further demonstrates the substantially ameliorated interphasial stability of heterostructure against the electrolyte, which is consistent with the improved cycling capability.

The long-term cycling stability of Mo-NC90 (730) was further evaluated in a full cell with graphite as the anode. The capacity ratio between the anode and cathode is approximately 1.1:1, as described in Fig. 4(f). Inset is the initial charge/discharge profiles of the half cells and full cell. The cycling performance of the graphite material is illustrated in Fig. S20. The Mo-NC90 (730)//graphite full cell exhibits a high specific capacity of 199.8 mAh g^{-1} with Coulombic efficiencies exceeding 99.8% and good capacity retention up to 70.5% after 1000 cycles at 1 C. This result once again proves the superiority of Mo-NC90 (730), benefiting from the protection effect of the pre-formed nanoscale heterostructure layer [50]. In order to highlight the effectiveness of this method, Fig. 4(g) and Table S5 compare the previously reported Ni-rich cathodes with Mo-NC90 (730), emphasizing its cycling stability and initial discharge capacity [37,41,51-58].

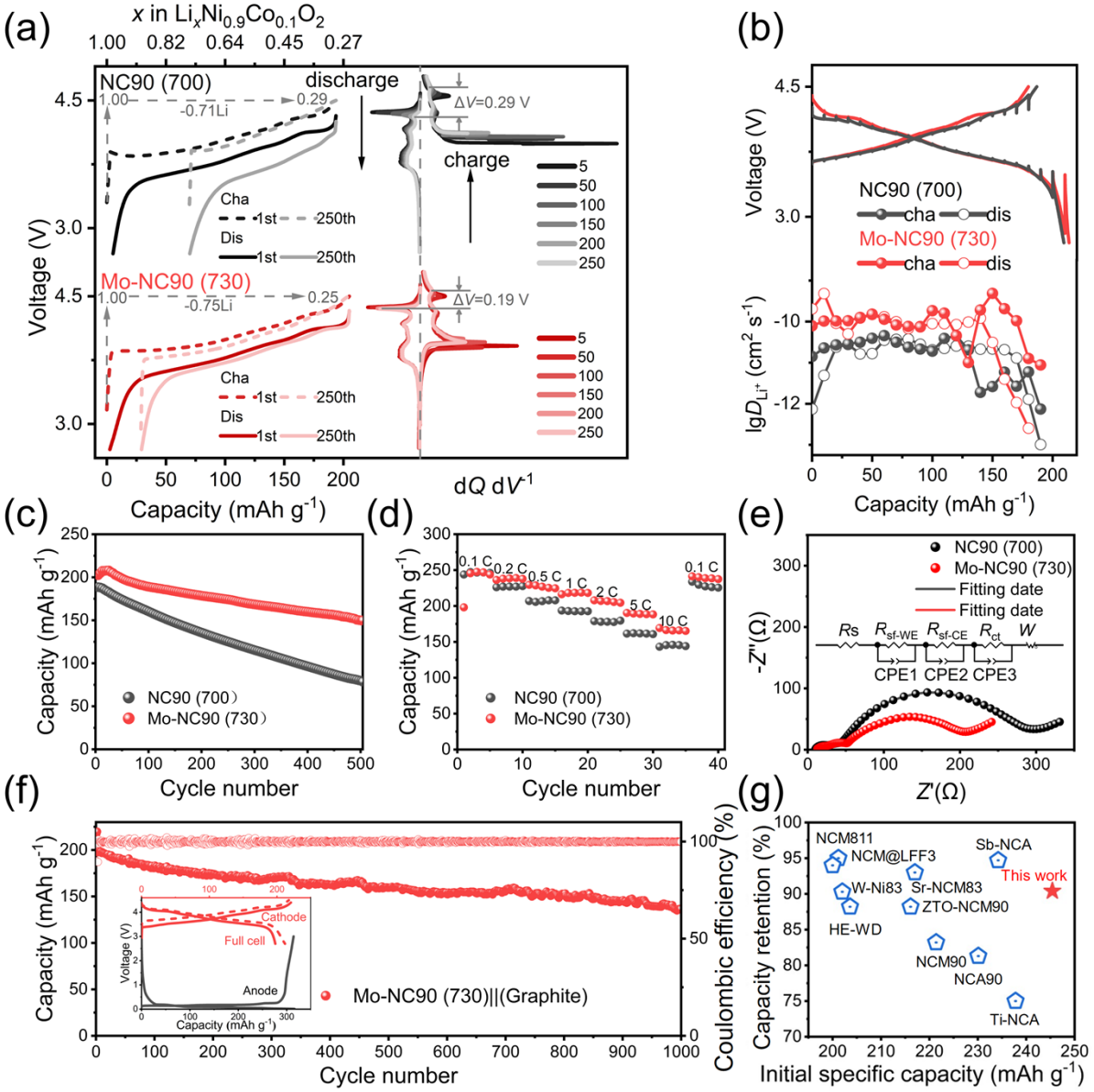

Fig. 4. (a) Charge-discharge profiles and dQ/dV curves of NC90 (700) and Mo-NC90 (730) at different cycles at 5/1 C. (b) Li^+ diffusion coefficient logarithm and the corresponding voltage profiles of NC90 (700) and Mo-NC90 (730) during charging-discharging process at the 500th cycle. (c) Cycling performance of different cathodes in half-cells at a charge/discharge rate of 5/1 C. (d) Rate performances at different current densities. (e) EIS spectra after 500 cycles in the frequency range of 0.1 MHz to 0.01 Hz. (f) Long-term cycling stability and Coulombic efficiency of Mo-NC90 (730)//graphite full cell cycled at 1 C between 2.7 and 4.4 V, and inset is the charge and discharge curves of the half and full cell. (g) Cycling stability after 100 cycles and initial specific capacity of Ni-rich cathode compared with reported works [31,47,51-58].

3.4. Characterization of structure evolution

In situ XRD characterization was conducted on NC90 (700) and Mo-NC90 (730) to detect the impact of heterostructure on the phase evolution and volume change during the charge-discharge process. Fig. 5(a–d) shows the voltage profile and contour plots of the characteristic diffraction peaks of (003), (101), (006), (012), and (104) for both materials during the in situ XRD process. The two cathodes both experience H1 (first hexagonal), H2 (second hexagonal), and H3 (third hexagonal) phase alteration during the charging up to 4.5 V [59]. The specific (003) peak is related to the changes of the lattice parameter along *c* directions. Accordingly, (003) gradually shifts to the low angle, indicating an increased *d*-spacing of the alkali metal layer due to the continuous expansion caused by electrostatic repulsion between adjacent oxygen layers [41]. When the voltage reaches approximately 4.15 V [60], the (003) peak shifts rapidly to higher angles, and the *c*-axis lattice parameter decreases sharply, corresponding to the H2 → H3 transition. The H2 → H3 transition is critical for maintaining reversible capacity during the phase alteration process [61]. It is observed that the (003) peak variation of Mo-NC90 (730) is 1.01°, much lower than 1.18° for NC90 (700). At the cut-off charge voltage (4.5 V), (101) and (104) peaks for Mo-NC90 (730) are 0.17° and 0.09° left compared to those for NC90 (700), indicating the improved stability of the bulk structure for the modified materials [59]. The fluctuation of the (104) peak around 4.5 V is attributed to the irreversible transformation from H2 phase to H3 phase (Fig. 5c). Additionally, Fig. 5(e and f) represents the variation of the calculated lattice parameter and cell volume during the charging process. The *c*-axis value variation for the modified cathode ($\Delta c = -4.94\%$) is less than that for NC90 (700) ($\Delta c = -6.10\%$). Thus, the volume change is significantly suppressed in the Mo-NC90 (730) cathode due to the mitigated lattice mismatch between the reconstructed heterophase surface and inner bulk at high delithiation depth. The designed heterostructure protective layer can restrain the harmful phase transformation and slow down the development of accumulated stress and crystal structure collapse [60]. XRD characterization of the cycled materials (Fig.

S21) reveals a significant reduction in the *I*(003)/*I*(104) intensity ratio for NC90 (700) after 500 cycles at 5 C, due to the formation of a large amount of rock-salt phase. Additionally, the (003) peak of NC90 (700) shifts 0.2° to higher angles compared to the pre-cycled material, which is greater than the 0.14° shift observed for Mo-NC90 (730). It indicates a greater volume change during cycling for the pristine material [62]. The (104) peak at around 45° of the cycled NC90 (700) splits, possibly due to the presence of some spinel phase [62]. The Mo-NC90 (730) sample shows fewer harmful phase transitions from the layered phase to spinel/rock-salt phases, demonstrating its excellent structural stability.

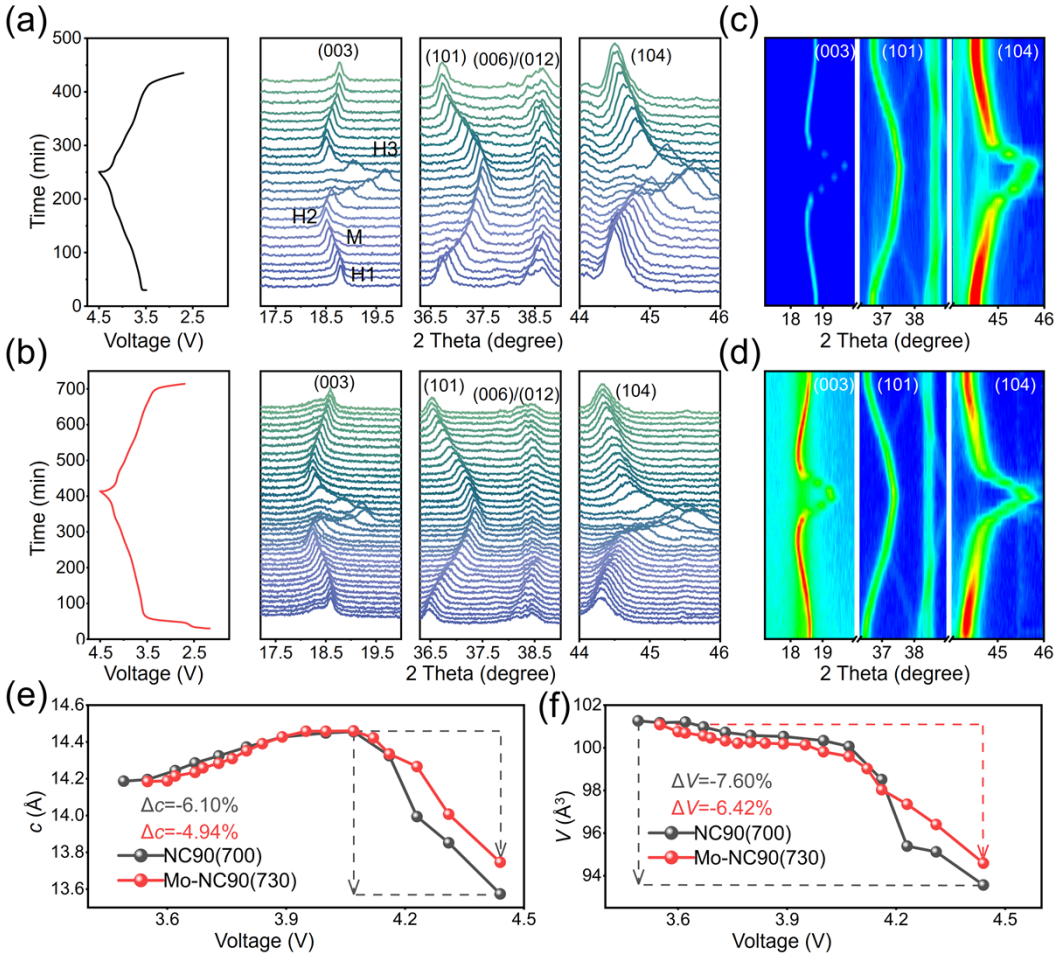

Fig. 5. In situ XRD characterization and corresponding charge-discharge curves of (a) NC90 (700) and (b) Mo-NC90 (730). The evolution of (003), (101), and (104) peaks during in situ XRD process for (c) NC90 (700) and (d) Mo-NC90 (730). The lattice parameter variation of the (e) *c*-axis and (f) volume for NC90 (700) and Mo-NC90 (730) during the charging process

at a current density of 0.2 C and at 2.7–4.5 V.

3.5. Interphase analysis

To further detect the deterioration mechanism of the cathode materials, the cycled cathodes were investigated using HRTEM and SEM, as shown in Fig. 6 and Fig. S22. The diameter of secondary particle for the cycled NC90 (700) is around 25 μm, whereas that for the cycled Mo-NC90 (730) maintains a diameter of 13 μm, similar to the fresh samples (Fig. S5). Besides, intragranular cracks appear in the cycled NC90 (700) particles (as the arrow points in Fig. S22). In contrast, the modified cathode retains mechanical integrity of particles, which effectively suppresses the continuous corrosion from the electrolyte.

Furthermore, as revealed by HRTEM (Fig. 6a and b), obvious differences of the cathode electrolyte interphase (CEI) layers on the two cathodes are observed. After 500 cycles, the pristine sample exhibits an uneven amorphous residual layer (3.8–6.5 nm) on the surface, while the Mo-NC90 sample has a more uniform layer with a thickness of only 1 nm. Besides, the NC90 (700) material also shows the seriously disordered rock-salt phases in the bulk as confirmed by FFT transformation (zone 1). These detrimental phase transitions from layered to rock-salt phases, accompanied by lattice oxygen loss and microcrack generation, severely deteriorate the cycling stability of NC90 (700) [63]. In contrast, Mo-NC90 (730) retains a well-maintained layered phase within the particles, indicating its superior structural stability and good cycling performance.

XPS analysis was conducted to further investigate the chemical compositions of the cycled cathode surfaces at different etching depths. In the O 1*s* spectrum (Fig. 6c), there is an abundant inorganic O signal (Li_2CO_3) on the surface of Mo-NC90 (730), but a mass of organic species ($ROCO_2Li$) appear on the surface of NC90 (700), indicating that more severe solvent decomposition occurs in NC90 (700), in agreement with the results of Li 1*s* spectra in Fig. S23 [64,65]. TM–O peak around 529.8 eV represents the lattice oxygen. The comparison between NC90 (700) and Mo-NC90 (730) on the TM–O peak further suggests the better lattice stability

and thinner CEI for Mo-NC90 (730) [66]. More coverage of carbonaceous components in NC90 (700), such as C–O, C=O, and OCO_2 in C 1*s* (Fig. 6d), largely originates from the decomposition of carbonate solvents in the electrolyte [64]. Sharp contrast can be observed in the F 1*s* spectra (Fig. 6d), where not only LiF component is higher in Mo-NC90 (730) than that in NC90 (700), but also the inner has higher inorganic F concentrations, demonstrating that the construction of the CEI layer in Mo-NC90 (730) is dominated by inorganic materials. These observations can also be evidenced by the statistical analysis of the corresponding content evolution of different chemical components/bonds related to O, C, and F, as shown in Fig. 6(e and f). As well known, the higher the concentration of inorganic chemistry accumulation on the CEI surface, the better the stability of the bulk structure for the cathode particles is. Consequently, the unfavorable decomposition reactions of electrolytes are effectively mitigated for Mo-NC90 (730) due to the protective effect of the heterostructure construction.

By comparing the two peaks representing Ni^{2+} and Ni^{3+} in the Ni 2*p* spectrum (Figs. S24 and S25), it is noted that Mo-NC90 (730) has more Ni^{2+} (35.7% vs. 26.5%) before cycling. However, NC90 (700) exhibits significantly higher content of Ni^{2+} (45%–51% at different etching times) than Mo-NC90 (730) (19%–38%) after cycling at different etching depths. It reveals that the serious phase transition occurs in the cycled NC90 (700). As shown in Fig. S26, more active materials clump and dissolve through the separator for NC90 (700). This demonstrates that the pre-constructed rock-salt phase at the interface effectively suppressed the dissolution of transition metals during cycling, resulting in the decreased loss of active elements.

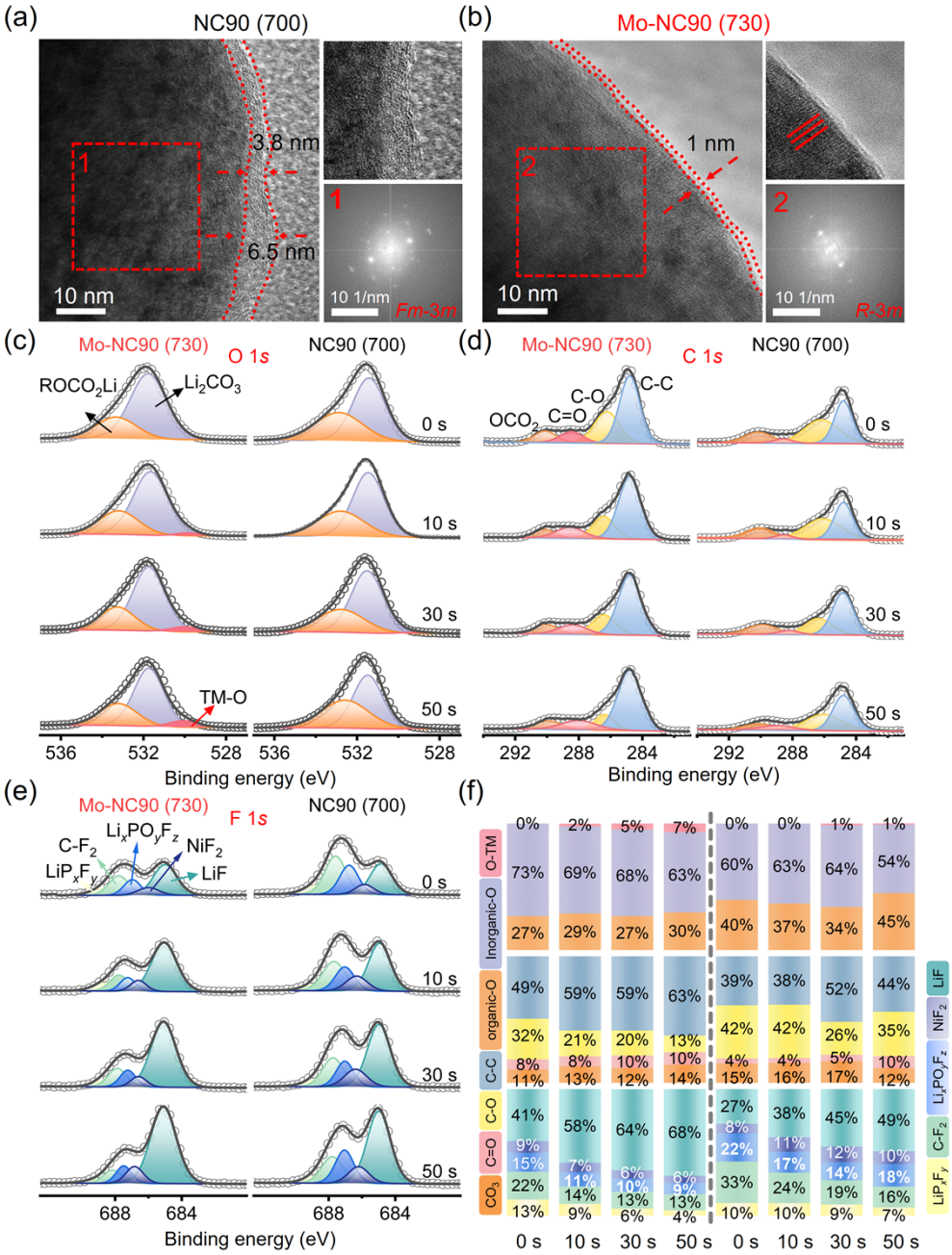

Fig. 6. HRTEM images of the cycled (a) NC90 (700) and (b) Mo-NC90 (730). XPS spectra of (c) O 1*s*, (d) C 1*s*, and (e) F 1*s* for cycled Mo-NC90 (730) and NC90 (700) after 500 cycles, and (f) the corresponding content evolution of different chemical components/bonds related to O, C, and F.

4. Conclusions

In this work, an epitaxial nanolayer of cation disordered phase on the $LiNi_{0.9}Co_{0.1}O_2$ surface is formed by incorporating high-valence Mo^{6+} during the lithiation process. The presence of

heterostructure construction promotes the Li^+ diffusion kinetics, reduces irreversible phase transitions, and enhances lattice oxygen stability and structure integrity. Besides, the detailed charge compensation mechanism of the optimized sample discloses that the average oxidation state of Ni is reduced, which induces more active Li^+ participating in the redox reactions. Furthermore, the volume change is significantly suppressed in the designed cathode due to the mitigated lattice mismatch between the reconstructed heterophase surface and inner bulk at high delithiation depth. As a result, the developed cathode materials exhibit an extraordinary discharge specific capacity of 245.4 mAh g^{-1} at 0.1 C, remarkable rate performance (169.3 mAh g^{-1} at 10 C) at 4.5 V, and high stable cycling life with the capacity retention of 70.5% after 1000 cycles in full cells at a high cut-off voltage of 4.4 V. This unique anchoring strategy of surface heterostructure on Ni-rich cathodes provides a new guidance to develop next-generation high-energy-density LIBs.

Supporting Information

Supplementary material associated with this article can be found, in the online version.

Acknowledgments

This work was financially supported by the National Natural Science Foundation of China (No. 52202228, 52402298), and funded by the Science Research Project of Hebei Education Department (No. BJK2022011), the Central Funds Guiding the Local Science and Technology Development of Hebei Province (No. 236Z4404G), the Beijing Tianjin Hebei Basic Research Cooperation Special Project (No. E2024202273), and the Science and Technology Correspondent Project of Tianjin (24YDTPJC00240). Dr. X.-G. S. and Prof. S. D. were supported by the U.S. Department of Energy's Office of Science, Office of Basic Energy Science, Materials Sciences and Engineering Division. The authors appreciate a portion of this research used resources at the Spallation Neutron Source, a DOE Office of Science User Facility operated by the Oak Ridge National Laboratory. This research also employed the resources of the BL14B beam at Shanghai Synchrotron Radiation Facility (SSRF) (Proposal

info: 2023-SSRF-PT-503737).

References

[1] F. Degen, M. Winter, D. Bendig, J. Tuebke, Nat. Energy 8 (2023) 1284-1295.
[2] F. Duffner, N. Kronemeyer, J. Tuebke, J. Leker, M. Winter, R. Schmuch, Nat. Energy 6 (2021) 123-134.
[3] J. Kim, Y. Kim, J. Yoo, G. Kwon, Y. Ko, K. Kang, Nat. Rev. Mater. 8 (2023) 54-70.
[4] W. Li, E. M. Erickson, A. Manthiram, Nat. Energy 5 (2020) 26-34.
[5] M. Zhang, D. A. Kitchaev, Z. Lebens-Higgins, J. Vinckeviciute, M. Zuba, P. J. Reeves, C. P. Grey, M. S. Whittingham, L. F. J. Piper, A. Van der Ven, Y. S. Meng, Nat. Rev. Mater. 7 (2022) 522-540.
[6] W. Li, S. Lee, A. Manthiram, Adv. Mater. 32 (2020) 2002718.
[7] C. Xu, K. Marker, J. Lee, A. Mahadevegowda, P. J. Reeves, S. J. Day, M. F. Groh, S. P. Emge, C. Ducati, B. Layla Mehdi, C. C. Tang, C. P. Grey, Nat. Mater. 20 (2021) 84-92.
[8] Y. Liao, H. Zhang, Y. Peng, Y. Hu, J. Liang, Z. Gong, Y. Wei, Y. Yang, Adv. Energy Mater. 14 (2024) 2304295.
[9] M. Cai, Y. Dong, M. Xie, W. Dong, C. Dong, P. Dai, H. Zhang, X. Wang, X. Sun, S. Zhang, M. Yoon, H. Xu, Y. Ge, J. Li, F. Huang, Nat. Energy 8 (2023) 159-168.
[10] U. H. Kim, H. H. Ryu, J. H. Kim, R. Mücke, P. Kaghazchi, C. S. Yoon, Y. K. Sun, Adv. Energy Mater. 9 (2019) 1803902.
[11] F. Wu, N. Liu, L. Chen, N. Li, J. Dong, Y. Lu, G. Tan, M. Xu, D. Cao, Y. Liu, Y. Chen, Y. Su, J. Energy Chem. 62 (2021) 351-358.
[12] N. Liu, L. Chen, H. Wang, J. Zhao, F. Gao, J. Liu, J. Dong, Y. Lu, N. Li, Q. Shi, Y. Su, F. Wu, Chem. Eng. J. 472 (2023) 145113.
[13] H. Zhang, J. Zhang, eTransportation 7 (2021) 100105.
[14] L. Lin, L. Zhang, S. Wang, F. Kang, B. Li, J. Mater. Chem. A 11 (2023) 7867-7897.
[15] F. Wu, N. Liu, L. Chen, Y. Su, G. Tan, L. Bao, Q. Zhang, Y. Lu, J. Wang, S. Chen, J. Tan, Nano Energy 59 (2019) 50-57.
[16] X. Tan, Z. Chen, T. Liu, Y. Zhang, M. Zhang, S. Li, W. Chu, K. Liu, P. Yang, F. Pan, Adv. Mater. 35 (2023) 2301096.
[17] S. Q. Lu, Q. Zhang, F. Meng, Y. N. Liu, J. Mao, S. Guo, M. Y. Qi, Y. S. Xu, Y. Qiao, S. D. Zhang, K. Jiang, L. Gu, Y. Xia, S. Chen, G. Chen, A. M. Cao, L. J. Wan, J. Am. Chem. Soc. 145 (2023) 7397-7407.
[18] U. H. Kim, D. W. Jun, K. J. Park, Q. Zhang, P. Kaghazchi, D. Aurbach, D. T. Major, G. Goobes, M. Dixit, N. Leifer, C. M. Wang, P. Yan, D. Ahn, K. H. Kim, C. S. Yoon, Y. K. Sun, Energy Environ. Sci. 11 (2018) 1271-1279.
[19] B. Xu, C. R. Fell, M. Chi, Y. S. Meng, Energy Environ. Sci. 4 (2011) 2223-2233.
[20] W. Zhao, J. Zheng, L. Zou, H. Jia, B. Liu, H. Wang, M. H. Engelhard, C. Wang, W. Xu, Y. Yang, J. G. Zhang, Adv. Energy Mater. 8 (2018) 1800297.
[21] Q. Lin, W. Guan, J. Meng, W. Huang, X. Wei, Y. Zeng, J. Li, Z. Zhang, Nano Energy 54 (2018) 313-321.
[22] A. A. Coelho, J. Appl. Cryst. 51 (2018) 210-218.
[23] Kresse, Hafner, Phys. Rev. B 47 (1993) 558-561.
[24] G. Kresse, J. Hafner, Phys. Rev. B 49 (1994) 14251-14269.
[25] J. P. Perdew, K. Burke, M. Ernzerhof, Phys. Rev. Lett. 77 (1996) 3865-3868.
[26] G. Kresse, D. Joubert, Phys. Rev. B 59 (1999) 1758-1775.
[27] S. Grimme, J. Antony, S. Ehrlich, H. Krieg, J. Chem. Phys. 132 (2010) 154104.
[28] W. Weppner, R.A. Huggins, J. Electrochem. Soc. 124 (1977) 1569.
[29] P. Kissinger, W.R. Heineman, Marcel Dekker 15 (1996) 550.
[30] Y. Zou, Y. Tang, Q. Zheng, H. Zhang, Y. Yan, J. Xue, S. Zhou, J. Xu, W. Yin, H. G.

Liao, Y. Qiao, J. Bao, S. G. Sun, Adv. Funct. Mater. 34 (2024) 2406068.
[31] G. T. Park, S. B. Kim, B. Namkoong, J. H. Ryu, J. I. Yoon, N. Y. Park, M. C. Kim, S. M. Han, F. Maglia, Y. K. Sun, Angew. Chem. Int. Ed. 62 (2023) e202314480.
[32] S. Guan, L. Tao, P. Tang, R. Fang, H. Wu, N. Piao, H. Yang, G. Hu, X. Geng, L. Li, B. An, F. Li, J. Energy Chem. 94 (2024) 449-457.
[33] Y. H. Luo, Q. L. Pan, H. X. Wei, Y. D. Huang, L. B. Tang, Z. Y. Wang, C. Yan, J. Mao, K. H. Dai, Q. Wu, X. H. Zhang, J. C. Zheng, Mater. Today 69 (2023) 54-65.
[34] D. Kong, J. Hu, Z. Chen, K. Song, C. Li, M. Weng, M. Li, R. Wang, T. Liu, J. Liu, M. Zhang, Y. Xiao, F. Pan, Adv. Energy Mater. 9 (2019) 1901756.
[35] Z. Zhang, X. Ding, X. Huang, X. He, Y. Gong, B. Xiao, J. Shen, X. Ou, Chem. Eng. J. 482 (2024) 148905.
[36] H. X. Wei, L. B. Tang, Y. D. Huang, Z. Y. Wang, Y. H. Luo, Z. J. He, C. Yan, J. Mao, K. H. Dai, J. C. Zheng, Mater. Today 51 (2021) 365-392.
[37] L. Ni, H. Chen, J. Gao, Y. Mei, H. Wang, W. Deng, G. Zou, H. Hou, X. Ji, ACS Nano 17 (2023) 12759-12773.
[38] H. Lu, S. Chu, J. Tian, Q. Wang, C. Sheng, C. Cheng, R. Liu, A. M. D'Angelo, W. K. Pang, L. Zhang, H. Zhou, S. Guo, Adv. Funct. Mater. 34 (2024) 2305470.
[39] Y. Sun, C. Wang, W. Huang, G. Zhao, L. Duan, Q. Liu, S. Wang, A. Fraser, H. Guo, X. Sun, Angew. Chem. Int. Ed. 62 (2023) e202300962.
[40] Q. Zhang, Q. Deng, W. Zhong, J. Li, Z. Wang, P. Dong, K. Huang, C. Yang, Adv. Funct. Mater. 33 (2023) 2301336.
[41] Z. Dai, H. Zhao, W. Chen, Q. Zhang, X. Song, G. He, Y. Zhao, X. Lu, Y. Bai, Adv. Funct. Mater. 32 (2022) 2206428.
[42] W. Lee, S. Muhammad, T. Kim, H. Kim, E. Lee, M. Jeong, S. Son, J. H. Ryou, W. S. Yoon, Adv. Energy Mater. 8 (2018) 1701788.
[43] Z. Cheng, B. Zhao, Y. J. Guo, L. Yu, B. Yuan, W. Hua, Y. X. Yin, S. Xu, B. Xiao, X. Han, P. F. Wang, Y. G. Guo, Adv. Energy Mater. 12 (2022) 2103461.
[44] J. Zhang, S. Wang, X. Yang, Y. Liu, Z. Wu, H. Li, S. Indris, H. Ehrenberg, W. Hua, Chem. Eng. J. 484 (2024) 149599.
[45] N.Y. Park, S.B. Kim, M.C. Kim, S.M. Han, D.H. Kim, M.S. Kim, Y.K. Sun, Adv. Energy Mater. 13 (2023) 2301530.
[46] H. Zhu, H. Yu, H. Jiang, Y. Hu, H. Jiang, C. Li, Chem. Eng. Sci. 217 (2020) 115518.
[47] H. H. Ryu, H. W. Lim, G. C. Kang, N. Y. Park, Y. K. Sun, ACS Energy Lett. 8 (2023) 1354-1361.
[48] K. Sada, S. Kmiec, A. Manthiram, Angew. Chem. Int. Ed. 63 (2024) e202403865.
[49] Z. Li, H. Yi, X. Li, P. Gao, Y. Zhu, ACS Appl. Mater. Interfaces 16 (2024) 28537-28549.
[50] S. Feng, Y. Lu, X. Lu, H. Chen, X. Wu, M. Wu, F. Xu, Z. Wen, Adv. Energy Mater. 14 (2024) 2303773.
[51] S. Jamil, R. Yu, Q. Wang, M. Fasehullah, Y. Huang, Z. Yang, X. Yang, X. Wang, J. Power Sources 473 (2020) 228597.
[52] L. Ni, H. Chen, W. Deng, B. Wang, J. Chen, Y. Mei, G. Zou, H. Hou, R. Guo, J. Xie, X. Ji, Adv. Energy Mater. 12 (2022) 2103757.
[53] Y. Chu, Y. Mu, L. Zou, Y. Hu, J. Cheng, B. Wu, M. Han, S. Xi, Q. Zhang, L. Zeng, Adv. Mater. 35 (2023) 2212308.
[54] Y. K. Hou, C. Li, D. Ren, F. He, K. Zhuang, S. Yin, G. Yuan, Y. Wang, Y. Guo, S. Liu, P. Sun, Z. Zhang, T. Tan, G. Zhu, L. Lu, X. Liu, M. Ouyang, Adv. Sci. 10 (2023) 2306347.
[55] Z. Tan, X. Chen, Y. Li, X. Xi, S. Hao, X. Li, X. Shen, Z. He, W. Zhao, Y. Yang, Adv. Funct. Mater. 33 (2023) 2215123.
[56] P. Liang, K. Qi, S. Chen, X. Ding, X. Wu, C. Wu, Y. Zhu, Angew. Chem. Int. Ed. 63

(2024) e202318186.
[57] L. Lin, L. Zhang, Z. Fu, J. Lou, Z. Gao, J. Wu, C. Li, C. Han, D. Zhou, Z. Wang, B. Li, Adv. Mater. 36 (2024) 2406175.
[58] Z. Tan, Y. Li, C. Lei, Y. Li, X. Xi, S. Jiang, F. Wu, Z. He, Small 20 (2024) 2305618.
[59] X. Cheng, X. Liu, L. Zhao, D. Zhang, J. Biao, Z. Chen, Y. Yuan, M. Liu, Y. B. He, F. Kang, Adv. Funct. Mater. 33 (2023) 2211171.
[60] Z. Huang, J. Yan, Z. Liu, W. Wang, Y. Tang, Z. Zhang, T. Yang, X. Wang, X. Li, Q. Kong, S. Lan, H. Zhu, Y. Ren, Q. Liu, Adv. Funct. Mater. 34 (2024) 2400956.
[61] X. He, J. Shen, B. Zhang, Z. Xiao, L. Ye, Q. Mao, Q. Zhong, X. Ou, Adv. Funct. Mater. 34 (2024) 2401300.
[62] J. Sun, X. Cao, H. Yang, P. He, M. A. Dato, J. Cabana, H. Zhou, Angew. Chem. Int. Ed. 61 (2022) e202207225.
[63] Y. Song, Y. Cui, L. Geng, B. Li, L. Ge, L. Zhou, Z. Qiu, J. Nan, W. Wu, H. Xu, X. Li, Z. Yan, Q. Xue, Y. Tang, W. Xing, Adv. Energy Mater. 14 (2024) 2303207.
[64] Q. Zhang, Y. Wang, Q. Deng, Y. Chu, P. Dong, C. Chen, Z. Wang, Z. Xia, C. Yang, Angew. Chem. Int. Ed. 63 (2024) e20240171.
[65] P. Bai, X. Ji, J. Zhang, W. Zhang, S. Hou, H. Su, M. Li, T. Deng, L. Cao, S. Liu, X. He, Y. Xu, C. Wang, Angew. Chem. Int. Ed. 61 (2022) e202202731.
[66] Y. Guo, C. Guo, P. Huang, Q. Han, F. Wang, H. Zhang, H. Liu, Y. C. Cao, Y. Yao, Y. Huang, eScience 3 (2023) 100091.

Graphical Abstract

We develop an ultrathin rock salt phase shell with conformal decoration on layered $LiNi_{0.9}Co_{0.1}O_2$ cathode material by inducing an appropriate amount of Li/Ni mixing via incorporation of high-valence Mo^{6+} during the lithiation process. The uniquely designed cathode materials exhibit a higher capacity (202.4 mAh g^{-1}), a lower polarization of 0.19 V, and remarkable capacity retention of 88% after 250 cycles.